

Molten salt attack on multilayer and functionally-graded YSZ coatings

Pablo Carpio^{1,*}, M. Dolores Salvador¹, Amparo Borrell¹, Lucia Navarro¹, Enrique Sánchez²

¹ Instituto de Tecnología de Materiales (ITM), Universitat Politècnica de València (UPV). Cami de Vera s/n, 46022 Valencia, Spain

² Instituto de Tecnología Cerámica (ITC), Universitat Jaume I (UJI). Campus Universitario Riu Sec, Av. Sos Baynat s/n, 12006 Castellón, Spain

* **Corresponding author**: Pablo Carpio

Address: Instituto de Tecnología de Materiales (ITM). Ciutat Politècnica de la Innovació, ed 8B semisótano, Cami de Vera s/n, 46022, Valencia, Spain.

Tel. number: (+34) 660806113

Fax number: (+34) 963877629

Email address: pabcarco@upv.es

Abstract

Thermal barrier coatings have been extensively studied in the last years in order to increase the operational temperature of the current gas turbines as well as to improve the coating lifetime. Many coating characteristics must be met to achieve these requirements (low thermal conductivity, high thermal fatigue resistance...); therefore, complex systems have been engineered for these purposes. One of the possibilities to optimise the different properties deals with the design of multilayer or functionally-graded coatings where various types of microstructures with different characteristics are combined.

One of the most important cause of gas turbines degradation relates to the attack of different type of particles which are suspended in the atmosphere (sand, fly ash...). These solid particles are molten at the operational temperatures and then, the molten salts chemically react with the coating. For this reason, the present research was focused on this type of attack.

In the present work, the molten salt attack of various YSZ coatings with multilayer and functionally-graded design was addressed. Two different type of microstructures were specifically combined for this design: the APS coating microstructure obtained from conventional (microstructured) powder and a bimodal structure with nanozones obtained from nanostructured feedstock. Besides, different salts were used to simulate different attack environments (desert sand and volcanic fly ash). Findings show that nanozones act as barrier against the penetration of molten salts toward deeper layer. However, a layer formed by nanozones can detach when the salt attack is too aggressive. Hence, functionally-graded coatings, where two types of microstructures are combined through the whole coating, become ideal to diminish the molten salt attack.

Keywords: c. chemical properties; d. ZrO₂; E. thermal applications; a. thermal spray deposition

1. Introduction

Thermal barrier coatings (TBC) are commonly utilized to protect the metallic parts of gas-turbines engines used to propel aircrafts and to generate electricity against extremely hot atmospheres. The most usual material for TBC is the yttria-stabilised zirconia (YSZ) because of its low thermal conductivity and good mechanical behaviour at high temperatures [1]. Regarding the technique, one of the most common is the atmospheric plasma spraying (APS) owing to its feasibility at industrial scale. The resultant APS coatings displays a laminar microstructure formed by flattened drops or splats with pores and cracks retained between them [2].

TBCs usually exhibit a limited lifetime due to the hard conditions which they must be subjected to (extreme temperatures, thermal fatigue, erosion...) [3]. One of these reasons deals with the attack of molten salts in contact with the coating surface. Solid particles (desert sand, volcanic fly ash...) which are suspended in the atmosphere are deposited onto the gas-turbine surface during the propelling. These particles are known as CMAS due to the main oxides they are usually composed of (CaO , MgO , Al_2O_3 , SiO_2). CMAS particles are molten at the operational temperatures and the resultant melt can chemically attack the coating and the substrate [4–7].

In the last years, some works have addressed several materials alternatives to the conventional YSZ to improve the different characteristics of the TBC, as the molten salt attack. One of the most promising materials is the zirconate with pyrochlore structure in general, and $\text{Gd}_2\text{Zr}_2\text{O}_7$ in particular, which exhibits an exceptionally low thermal conductivity and a good chemical resistance [5,7,8]. However, its low coefficient of thermal expansion causes that these coatings present poor thermal fatigue resistance. Another alternative consists in designing of several types of microstructures which lead to develop different characteristics for the TBC [2,9].

Nanostructured materials have been extensively studied due to their enhanced properties compared to their respective conventional ones. In the case of TBC developed by APS, nanoparticles must be enlarged in nanostructured agglomerates to become the feedstock sprayable inside the plasma plume. The resultant coating displays the so-called bimodal microstructure formed by unmolten zones, where the initial nanostructure is partially retained, rounded by a matrix of molten splats. The unmolten zones lead to a reduction of the thermal conductivity and an improvement of the thermal fatigue resistance. However, some properties, such as the hardness, can be compromised [11–13].

In order to optimise the properties of different kind of materials and/or microstructures, multilayer and functionally-graded coatings can be designed where both kind of microstructures/compositions are combined. The multilayer coatings consist in depositing two layers with different microstructure while the

variation of microstructure/composition is gradual in the case of functionally-graded coatings. Previous works have addressed this type of coatings to optimise the mechanical and thermal properties of the TBC. Thus, this functionally-graded coatings display high lifetime because the generation of tensions during the thermal fatigue diminishes due to the gradual microstructure change through the coating [14–19]. Once the improvement of multilayer and functionally-graded coatings have been demonstrated in terms of mechanical and thermal behaviour, the objective of the present work was the evaluation of the chemical attack resistance of this type of coatings.

2. Experimental

2.1. Coating preparation

Two commercial yttria-stabilised zirconia (YSZ) powders were used as feedstocks for obtaining the conventional and the nanostructured layers. On one hand, the conventional powder (Metco 204NS, Oerlikon-Metco, Switzerland) consisted in hollow spheres (HOSP) with a average granule size of 55 μm , granule specific mass of 4500 kg/m^3 and a amount of dopant of 8 wt% Y_2O_3 . On the other hand, the nanostructured powder (NanoxTM S4007, Inframat Advanced Materials, USA) was made up of nanostructured porous agglomerates with an average granule size of 160 μm , granule specific mass of 2320 kg/m^3 and an amount of dopant of 7 wt% Y_2O_3 . The feedstock characterisation has been set out in a previous work [20].

The different YSZ layers were deposited by atmospheric plasma spraying (APS) torch (F4-MB, Oerlikon-Metco, Switzerland) operated by a 6-axes robot (IRB 1400, ABB, Switzerland). Besides, a bond coat (Amdry 997, Oerlikon-Metco, Switzerland) was deposited between the substrate and the ceramic layers. Two independent feed systems (one for each powder) were used to develop the multilayer and functionally-graded coatings. More information about the spraying parameters as well as the deposition process can be consulted in [14,20].

Two multilayer coatings (M1 and M2) and two functionally-graded ones (G1 and G2) were designed in this work. Multilayer coatings were formed by two different YSZ layers: one conventional and another nanostructured. As set out in a previous research [14,15], the conventional layer was formed by molten lamellas or splats with small pores embedded between these splats while the nanostructured layer consisted in an unmolten zones called nanozones, where the starting nanostructure of the feedstock is retained, rounded by a matrix of molten splats. The conventional layer was located between the bond coat and the nanostructured layer in M1 coating while conventional and nanostructured layers were exchanged in M2 coating. Regarding functionally-graded coatings,

these were made up of five YSZ layers with different conventional/nanostructured ratios changing the proportion the gradually along their thickness. In the case of G1 the conventional layer laid in bottom and the nanostructured layer in the top while for G2 the same layers were deposited in the opposite order. A scheme about the design of the four coatings is displayed in Fig. 1.

2.2 CMAS synthesis and characterisation

Two CMAS compositions were studied in the present work: one simulates the composition of the desert sand while another simulates the fly ash, called CMAS-1 and CMAS-2 respectively. The compositions, which are shown in Table 1, were taken from previous works [5,6].

Simulated CMAS glass was prepared from reagent-grade dry powders of SiO₂, CaCO₃, Al₂O₃, MgO, Na₂O, K₂O and Fe₂O₃ (all supplied from Sigma-Aldrich, USA) which were mixed in the appropriate proportions. These mixtures were molten in an electrical furnace at 1550 °C for 1 h and then, the melt was quenched in water. The resultant amorphous material was characterised in order to predict the thermal behaviour during the attack to the coating. A differential thermal analysis (DTA) tests (TGA/SDTA 851e, Mettler Toledo, Switzerland) were carried out using a platinum crucible in air atmosphere, with a heating rate of 10 °C min⁻¹ until a maximum temperature of 1500 °C. Besides, the crystalline phases were identified by Raman spectroscopy (NRS-3100, Jasco, USA) before and after thermal treating the CMAS. A 785 nm laser wavelength excitation was used in the Raman measurements besides the spectra background was subtracted because the fluorescence effect was important and dissimilar among the different samples.

2.3 Study of the CMAS attack

CMAS suspensions, with ethanol as dispersant, were prepared by an attrition mill () to deposit correctly the CMAS onto the coating surface. The glass was milled with 1 mm alumina balls for 30 min at 1000 rev/min and the resultant suspension was sieved at 63 µm mesh size to remove the coarse CMAS particles. The resultant suspension, with a solid loading of 20 wt.%, was stable and it displayed an ideal rheology to spray the CMAS using an airbrush. Then, the coatings with CMAS were dried to remove the ethanol prior to the thermal treatment. It was corroborated that the amount of CMAS onto the coatings was 20 mg/cm². The thermal treatment was realised in an electrical furnace (Thermolyne type 46100, Thermo Fischer Scientific, USA) at a temperature of 1250 °C for 1 h. The temperature was selected from the thermal characterisation performed in the CMAS.

As-sprayed and CMAS-attacked coatings were microstructurally characterised to describe the CMAS attack. In addition, thermally-treated coatings without CMAS were also characterised to evaluate sintering changes. Microstructure observation was realised by field-emission scanning electron microscopy (ULTRA 55, ZEISS, Germany) on cross-section samples embedded in a polyacrylate resin, metallographically prepared and coated with carbon by sputtering. Besides, an energy disperse X-ray microanalysis (Oxford Instruments, United Kingdom) associated to the FE-SEM allows realising chemical analysis in different zones of the coating. The crystalline changes during the attack were also identified by Raman spectroscopy following the same methodology used to characterise the CMAS glass.

3. Results and discussion

3.1 CMAS characterisation

A differential thermal analysis permits to know the behaviour of the CMAS during the temperature changes when it attacks the turbines. Fig. 2 displays DTA of both CMAS glasses. In the case of CMAS 1, an endothermic peak was observed at 910 °C which corresponds to vitreous transition, an exothermic peak around 1000 °C which corresponds to the crystallization and other endothermic peak at -1250 °C associated with the melting point. The thermal behaviour of CMAS-2 was similar, occurring the thermal phenomena at similar temperatures but the melting process was more energetic in the case of CMAS-2. The temperature treatment to evaluate the CMAS attack was selected at the beginning of CMAS melting because the attack commence to be important after this point (1250 °C). In preliminary results it was observed the damage was insignificant when the CMAS attack took place at lower temperatures. Finally, the crystalline formation after treating the CMAS glass a 1250 °C and subsequent slow cooling, following the same thermal treatment that the coating attacked, was detected by Raman spectra. The glass was mainly amorphous although the spectra shown in Fig. 3 reveals some peaks which correspond to the wollastonite crystallization (CaSiO_4) [21].

Other properties of the CMAS were estimated in order to predict the damage that each material can produce. In this sense, viscosity was calculated using the model validated by Giordano et al. for silicate melts at different temperatures [22] while another model proposed by Kucuk et al. was utilised to estimate the surface tension [23]. The viscosity and surface tension are shown in Table 2. As it can be appreciated surface tension is similar but CMAS-2 is less viscous than CMAS-1. It is reasonable because CMAS-2 contains higher fluxing oxide amount such as Na_2O , K_2O or Fe_2O_3 which facilitate the melt formation. It means that CMAS-2 is expected to display further ability to penetrate more easily into the coating. In addition to above properties, optical basicity was also

estimated averaging the basicity values of each component forming the glass [4]. This concept, based in Lewis acid-base theory, permits to predict the chemical activity of the glasses. This way the higher the optical basicity mismatch between glass and coating the higher chemical activity is expected. The optical basicity of the 8 mol% yttria-stabilized zirconia is 0.87 therefore CMAS-2 exhibited a slightly higher basicity respect the coating. Nevertheless, the optical basicities were not significantly dissimilar but a different behaviour in the CMAS attack can be expected because of their viscosities which were very different.

3.2 Study of the CMAS attack

3.2.1 Description of the CMAS attack

The assessment of the CMAS attack was basically realised comparing the coating microstructures. First, the coatings thermally treated with and without the CMAS were compared in order to evaluate if the damage was originated by the CMAS attack or just by the thermal treatment produced during the test. Fig. 4 displays M2 coating (conventional layer onto nanostructured layer) comparing the different treatments (as-sprayed, thermally treated and attacked by the CMAS). The nanozones were observed in the bottom of the coating where the nanostructured layer was located. Nevertheless, differences in these nanozones can be detected [14,20]. The nanozones in the as-sprayed coating were quite porous and the original particles which formed the starting feedstocks can be distinguished. In the case of thermally-treated coating without the CMAS, these nanozones were less porous and some of these particles coalesced or are linked by a neck owing to the sintering process [13]. Nevertheless, the coalescence was negligible in the nanozones of coatings attacked by the CMAS because the melt penetrated into the nanozones surrounding the particles before the sintering process occurred. It was corroborated by EDX that the dark zone around the particles displays a rich content in CMAS oxides.

In addition to the differences in the nanozones, zones chemically attacked were observed in the attacked coating which cannot be detected in the other cases. This zone is magnified in Fig. 5 and the chemical composition in several regions is also displayed in Table 3. An EDX analysis in the coating crack (marked by a star in Fig. 5) confirmed they are composed mainly by CMAS although ZrO_2 was detected because the solid matrix around the cracks was inside the influence zone of the EDX analysis. Therefore it means CMAS melt penetrated into the coating through the cracks. Besides, little channels perpendicular to the cracks were formed because CMAS melt reacted and dissolved the solid matrix (marked by a diamond in Fig. 5) [24]. Moreover, a yttria reduction was observed in the solid matrix (from 7-8 wt.% in as-sprayed coating to 6 wt.% in attacked

coating) as well as a significant presence of yttria (around 5 wt.%) in the CMAS melt zone, concluding that an yttria transport or lixiviation from the solid matrix (bright zones) toward the CMAS melt (dark zones) was observed [7]. The yttria content reduction inside the solid matrix can imply a loss of crystalline stability which was analysed by Raman spectroscopy.

3.2.2 Effects of the CMAS-1

CMAS unevenly attacked the coating due to the different microstructure features. CMAS oxides were mainly appreciated in the layers with nanozones because these layers were more porous therefore easier to be penetrated, as it can be observed in Table 4. However, CMAS penetration into the coating depended in turn on the distribution of these nanozones. Moreover, chemical attack also leads to different microstructural changes among the coatings (Fig. 6). On one hand comparing multilayer coatings (M1 and M2), the zones chemically attacked as described in Fig. 5 practically took up the whole conventional layer in M2 coating whereas these zones were unclearly visible in M1 coating. Besides, CMAS oxide content was similar in the nanostructured layers but the conventional layer in M1 coating displayed lower CMAS content than that of its respective layer in M2 coating. It means that nanostructured layer acts as a reservoir of CMAS melt which prefers to react with zones displaying higher specific surface as the nanozones. Hence, the nanostructured layer behaved as a barrier against CMAS penetration.

On the other hand, the functionally-graded coatings (G1 and G2) showed a behaviour moderately improved respect their multilayer counterparts since CMAS penetration into the coating was slightly lower. Consequently, the combination of the two microstructures (conventional and nanostructured) acts much better as barrier than each microstructure separately. It can be caused by two opposite effects which are displayed by the nanozones. Thus nanozones are quite porous therefore CMAS melt can easily penetrate despite these zones acted as a barrier as set out above. Therefore the result of combining conventional and nanostructured layers involves the presence of nanozones in the coating while the porosity is reduced and hence an improved behaviour observed.

3.2.3 Effects of the CMAS-2

In Fig. 7 it can be observed that CMAS-2 attack was more aggressive, as predicted. In fact, top layer in the coating M1 (nanostructured layer) was completely detached. This is because the porosity in nanostructured layer was very high increasing the reactivity of the melt. As a result the melt reacted quickly with the nanozones before it can distribute towards other regions of the coating. The nanozones took a large portion of the nanostructured layer whose

disintegration produces the layer detachment. In the case of M2 coating, the conventional layer in the top did not block the access of the melt toward the bottom layer because the melt viscosity is too low and consequently the melt rapidly flowed through the cracks. Once nanostructured layer was detached then the full coating collapsed. Hence, it can be concluded that it is convenient to deposit the nanostructured layer onto the conventional layer as observed with the CMAS-1 attack despite the fact that the lower hardness of the nanostructured layer can give rise to an impaired erosion resistance [15].

CMAS-2 attack was catastrophic for multilayer coatings but the effect was different in functionally-graded coatings since no detachment of any layer was observed. Besides, the amount of CMAS oxides detected by EDX analysis was lower than that of CMAS-1 although it was slightly higher in G2 coating. The preference to attack the nanozones occurs with both CMAS melts but it is more important in CMAS-2. The nanostructured layer displays huge nanozones and the attack toward these zones causes the depletion of that layer. However, nanozones combined with a bulk matrix prevent the layer depletion while the nanozones keep performing its function as barrier. Definitely, the combination nanostructured and conventional microstructures responds better against any type of CMAS attack.

The chemical attack mechanism of the CMAS-2 was similar to that of the other CMAS melt. In this case, less zones chemically attacked, as those displayed in Fig. 8, are observed in spite of the higher attack intensity. Likewise, the sum of the CMAS oxides in these coatings was lower than that of coatings attacked by CMAS-1 (Table 5). This is because some CMAS melt reacted with the detached areas leading to material removal. Nevertheless, an attack intensity increment was confirmed when the chemical analysis of these chemical-attacked zones was performed (Table 3). Higher amount of yttria was observed in the cracks where the CMAS melt was located as well as less presence of this oxide in the molten areas. Consequently, a higher yttria lixiviation occurred which can affect zirconia crystallisation. Besides, significant calcium oxide content was appreciated in the solid matrix, hence calcium cations from the CMAS were introduced in the crystalline lattice. Whereas calcium is another dopant which can stabilise the tetragonal zirconia phase its effect is lower than that of yttria, consequently the impact on the tetragonal stabilization in these coatings should be unimportant [25].

3.2.4 Study of the crystalline phases by Raman

The Raman spectra analysis in different areas of the coatings, as well as among coatings with the same treatment, were all of them similar. A spectrum of M1 coating with different treatments (as-sprayed, thermally treated and attacked by CMAS), obtained in the molten matrix, is displayed in Fig. 9.

Tetragonal zirconia was the only crystalline phase detected in any area of the coatings whereas wollastonite, an original phase from the thermally-treated CMAS was imperceptible. Despite the peaks in all spectra were similar, the position of these peaks was slightly shifted. It means that the nature of the bonds in the crystalline lattice were similar but changes in the local symmetry must exist. As addressed in previous works a shift of the Raman band toward higher wavelength represents an increment of the oxygen displacement, i.e a lower stabilisation of the tetragonal phase because of a decreasing in the amount of stabilizer ions (Y^{3+}) [26]. It agrees with the EDX analysis so that in coatings chemically attacked with CMAS, especially CMAS-2, a lixiviation of yttrium cations observed gave rise to a lower tetragonality in zirconia phase. The consequence was that the chemically attacked coatings exhibited a worse lifetime because a lower tetragonality means a catastrophic martensitic change from tetragonal to monoclinic phase occurs at lower temperatures and/or exposure times [27]. Another possibility to explain this peak translation deals with the stress generation during the thermal treatment [28]. It explains that thermally-treated coating spectrum was displaced. However, this displacement was lower than that of the coatings attacked by CMAS, consequently thermal stresses as well as tetragonality lose should explain the spectrum displacement.

4. Conclusion

The resistance of TBC against two different CMAS salts was studied, one simulating the desert sand and the other the volcanic ash. CMAS characterisation allowed to conclude that both glasses melt at 1250 °C, for that reason the attacks against the coatings were realized at this temperature. CMAS-2 displayed lower viscosity at high temperature therefore it is expected this molten salt can attack faster a given coating.

The effect of the coating CMAS resistance was addressed in coatings combining different type of microstructures: a conventional (from microstructured powder feedstocks) formed by molten splats and nanostructured (from nanostructured powder feedstocks) with porous nanozones embedded in a molten matrix. For this goal, four coatings (two multilayer and two functionally-graded), where both type of microstructures were combined, were attacked with the two salts. It was observed the CMAS preferred to attack the nanozones because of their higher specific surface. Therefore, nanostructured layers were more damaged, and even they were detached when the salt was more aggressive (CMAS-2). It implied that in coatings where the nanostructured layer was located in the bottom, the top layer was more damaged, or the fully detachment of the coating in the case of CMAS-2 attack. Another consequence of the corrosion attack was a worse

crystalline phase stability, corroborated by Raman spectroscopy, owing to a lixiviation of yttrium cations from the coating to the CMAS melt.

Regarding the functionally-graded coatings, the CMAS attack was reduced. In fact, the layer detachment was not observed, besides CMAS oxides content detected in the coatings after the test was lower. The reason is based on the fact that the combination of conventional and nanostructured microstructures allows to obtain nanozones but with a porosity decrease, optimising the barrier effect of the CMAS. As a conclusion, the functionally-graded coatings displays a better behaviour against the CMAS corrosion compared to multilayer coatings.

Acknowledgment

This work has been supported by the Spanish Ministry of Economy and Competitiveness (project MAT2015-67586-C3-R) as well as A. Borrell and L. Navarro thanks for their post-doc (RyC-2016-20915) and pre-doc (BES-2016-077792) contracts respectively. P. Carpio acknowledges the Valencia Government for his post-doc contract (APOSTD/2016/040).

References

- [1] D.R. Clarke, M. Oechsner, N.P. Padture, Thermal-barrier coatings for more efficient gas-turbine engines, *MRS Bull.* 37 (2012) 891–898.
- [2] G. Mauer, M.O. Jarligo, D.E. Mack, R. Vassen, Plasma-sprayed thermal barrier coatings: New materials, processing issues, and Solutions, *J. Therm. Spray Technol.* 22 (2013) 646–658.
- [3] V. Kumar, K. Balasubramanian, Progress update on failure mechanisms of advanced thermal barrier coatings: A review, *Prog. Org. Coatings.* 90 (2016) 54–82.
- [4] A.R. Krause, B.S. Senturk, H.F. Garces, G. Dwivedi, A.L. Ortiz, S. Sampath, N.P. Padture, 2ZrO₂·Y₂O₃ thermal barrier coatings resistant to degradation by molten CMAS: Part I, Optical basicity considerations and processing, *J. Am. Ceram. Soc.* 97 (2014) 3943–3949.
- [5] J.M. Drexler, A.L. Ortiz, N.P. Padture, Composition effects of thermal barrier coating ceramics on their interaction with molten Ca-Mg-Al-silicate (CMAS) glass, *Acta Mater.* 60 (2012) 5437–5447.
- [6] J.M. Drexler, K. Shinoda, A.L. Ortiz, D. Li, A.L. Vasiliev, A.D. Gledhill, S. Sampath, N.P. Padture, Air-plasma-sprayed thermal barrier coatings that are resistant to high-temperature attack by glassy deposits, *Acta Mater.* 58 (2010) 6835–6844.
- [7] R. Kumar, E. Jordan, M. Gell, J. Roth, C. Jiang, J. Wang, S. Rommel,

- CMAS behavior of yttrium aluminum garnet (YAG) and yttria-stabilized zirconia (YSZ) thermal barrier coatings, *Surf. Coatings Technol.* 327 (2017) 126–138.
- [8] J.M. Drexler, C.H. Chen, A.D. Gledhill, K. Shinoda, S. Sampath, N.P. Padture, Plasma sprayed gadolinium zirconate thermal barrier coatings that are resistant to damage by molten Ca-Mg-Al-silicate glass, *Surf. Coatings Technol.* 206 (2012) 3911–3916.
- [9] S. Mahade, K.P. Jonnalagadda, N. Curry, X.H. Li, S. Björklund, N. Markocsan, P. Nylén, R.L. Peng, Engineered architectures of gadolinium zirconate based thermal barrier coatings subjected to hot corrosion test, *Surf. Coatings Technol.* 328 (2017) 361–370.
- [10] S. Sivakumar, K. Praveen, G. Shanmugavelayutham, Preparation and thermophysical properties of plasma sprayed lanthanum zirconate, *Mater. Chem. Phys.* 204 (2018) 67–71.
- [11] P. Fauchais, G. Montavon, R.S. Lima, B.R. Marple, Engineering a new class of thermal spray nano-based microstructures from agglomerated nanostructured particles, suspensions and solutions: an invited review, *J. Phys. D: Appl. Phys.* 44 (2011) 93001.
- [12] R. Ghasemi, R. Shoja-Razavi, R. Mozafarinia, H. Jamali, Comparison of microstructure and mechanical properties of plasma-sprayed nanostructured and conventional yttria stabilized zirconia thermal barrier coatings, *Ceram. Int.* 39 (2013) 8805–8813.
- [13] Q. Yu, A. Rauf, N. Wang, C. Zhou, Thermal properties of plasma-sprayed thermal barrier coating with bimodal structure, *Ceram. Int.* 37 (2011) 1093–1099.
- [14] P. Carpio, E. Bannier, M.D. Salvador, R. Benavente, E. Sánchez, Multilayer and Particle Size-Graded YSZ Coatings Obtained by Plasma Spraying of Micro- and Nanostructured Feedstocks, *J. Therm. Spray Technol.* 23 (2014) 1362–1372.
- [15] P. Carpio, E. Rayón, M.D. Salvador, L. Lusvarghi, E. Sánchez, Mechanical Properties of Double-Layer and Graded Composite Coatings of YSZ Obtained by Atmospheric Plasma Spraying, *J. Therm. Spray Technol.* 25 (2016) 778–787.
- [16] S. Nath, I. Manna, J.D. Majumdar, Kinetics and mechanism of isothermal oxidation of compositionally graded yttria stabilized zirconia (YSZ) based thermal barrier coating, *Corros. Sci.* 88 (2014) 10–22.
- [17] D. Chen, E.H. Jordan, M. Gell, Effect of solution concentration on splat formation and coating microstructure using the solution precursor plasma spray process, *Surf. Coatings Technol.* 202 (2008) 2132–2138.
- [18] X. Chen, L. Gu, B. Zou, Y. Wang, X. Cao, New functionally graded thermal barrier coating system based on LaMgAl 11O 19/YSZ prepared by air plasma spraying, *Surf. Coatings Technol.* 206 (2012) 2265–2274.

- [19] V. Viswanathan, G. Dwivedi, S. Sampath, Engineered Multilayer Thermal Barrier Coatings for Enhanced Durability and Functional Performance, *J. Am. Ceram. Soc.* 97 (2014) 2770–2778.
- [20] P. Carpio, E. Bannier, A. Borrell, M.D. Salvador, E. Sánchez, Influence of atmospheric plasma spray parameters on YSZ coatings obtained from micro and nanostructured feedstocks, *Bol. La Soc. Esp. Ceram. Y Vidr.* 53 (2014).
- [21] P. Colomban, V. Milande, H. Lucas, On-site Raman analysis of Medici porcelain, *J. Raman Spectrosc.* 35 (2004) 68–72.
- [22] D. Giordano, J.K. Russell, D.B. Dingwell, Viscosity of magmatic liquids: A model, *Earth Planet. Sci. Lett.* 271 (2008) 123–134.
- [23] A. Kucuk, A. Clare, L. Jones, An estimation of the surface tension for silicate glass melts at 1400°C using statistical analysis, *Glas. Technol.* 40 (1999) 149–153.
- [24] A.D. Gledhill, K.M. Reddy, J.M. Drexler, K. Shinoda, S. Sampath, N.P. Padture, Mitigation of damage from molten fly ash to air-plasma-sprayed thermal barrier coatings, *Mater. Sci. Eng. A.* 528 (2011) 7214–7221.
- [25] A.K. Bhattacharya, P. Reinhard, W. Steurer, V. Shklover, Calcia-doped yttria-stabilized zirconia for thermal barrier coatings: Synthesis and characterization, *J. Mater. Sci.* 46 (2011) 5709–5714.
- [26] C. Viazzi, J.P. Bonino, F. Ansart, A. Barnabé, Structural study of metastable tetragonal YSZ powders produced via a sol-gel route, *J. Alloys Compd.* 452 (2008) 377–383. doi:10.1016/j.jallcom.2006.10.155.
- [27] G. Witz, V. Shklover, W. Steurer, S. Bachegowda, H.-P. Bossmann, Phase evolution in yttria-stabilized zirconia thermal barrier coatings studied by rietveld refinement of X-ray powder diffraction patterns, *J. Am. Ceram. Soc.* 90 (2007) 2935–2940.
- [28] M. Tanaka, M. Hasegawa, A.F. Dericioglu, Y. Kagawa, Measurement of residual stress in air plasma-sprayed Y₂O₃-ZrO₂ thermal barrier coating system using micro-Raman spectroscopy, *Mater. Sci. Eng. A.* 419 (2006) 262–268.

Table list

Table 1. Chemical composition of both CMAS studied in the present work.

		SiO ₂	CaO	Al ₂ O ₃	MgO	Na ₂ O	K ₂ O	Fe ₂ O ₃
CMAS-1 [5]	mol%	51.5	39.2	7.1	3.5			
	wt%	52.3	37.1	7.1	3.5			
CMAS-2 [6]	mol%	50.0	38.0	5.0	4.0	1.0	1.0	1.0
	wt%	49.6	35.2	3.3	6.7	1.0	1.6	2.6

Table 2. Viscosity (μ), surface tension (σ) and optical basicity (\wedge) of the CMAS melts.

	μ (Pa·s)	σ (N/m)	\wedge
CMAS-1	101	426	0.70
CMAS-2	40	423	0.68

Table 3. Punctual EDX analysis (wt%) in different zones of the region attacked by CMAS. CMAS-1 and CMAS-2 attack are displayed in fig. 5 and fig. 8 respectively.

Attacked	Zone	ZrO ₂	Y ₂ O ₃	SiO ₂	CaO	Al ₂ O ₃	MgO	Na ₂ O	K ₂ O	Fe ₂ O ₃	Σ CMAS
CMAS-1 (M2 coating)	Solid matrix	93.8	6.2	-	-	-	-	-	-	-	-
	Crack/melt	6.2	4.8	48.7	25.2	12.8	2.3	-	-	-	89.1
CMAS-2 (M1 coating)	Solid matrix	92.2	5.3	-	2.5	-	-	-	-	-	(2.5)*
	Crack/melt	6.0	5.1	43.2	27.4	14.5	1.3	0.7	0.6	1.3	6.0

(*) CaO is introduced in the crystalline lattice and it really doesn't constitute a part of CMAS glass.

Table 4. EDX analysis (wt%) of the coatings attacked by CMAS-1 in half top region and half bottom region. The type of layer (c: conventional; n: nanostructured) is pointed between parenthesis.

	Layer/level	ZrO ₂	Y ₂ O ₃	SiO ₂	CaO	Al ₂ O ₃	MgO	Σ CMAS
M1	Top (n)	74.7	3.2	10.8	8.4	3.2	0.4	22.7
	Bottom (c)	81.5	4.1	6.4	5.5	2.2	0.3	14.4
M2	Top (c)	86.5	2.2	4.1	4.1	1.0	0.2	9.4
	Bottom (n)	78.1	2.1	9.2	6.8	2.8	0.5	19.2
G1	Top (n)	76.8	1.5	10.9	2.8	7.5	0.6	21.7
	Bottom (c)	86.2	2.3	5.8	4.2	1.1	0.4	11.5
G2	Top (c)	80.3	4.7	7.2	5.3	2.1	0.4	15.0
	Bottom (n)	81.4	4.8	6.3	4.6	2.5	0.4	13.8

Table 5. EDX analysis (wt%) of the coatings attacked by CMAS-2 in half top region and half bottom region. The type of layer (c: conventional; n: nanostructured) is pointed between parenthesis.

	Layer/ level	ZrO ₂	Y ₂ O ₃	SiO ₂	CaO	Al ₂ O ₃	MgO	Na ₂ O	K ₂ O	Fe ₂ O ₃	ΣCMAS
M1	Top (n)	-	-	-	-	-	-	-	-	-	-
	Bottom (c)	86.8	6.5	2.5	2.4	1.4	0.2	0.1	-	0.2	6.7
M2	Top (c)	-	-	-	-	-	-	-	-	-	-
	Bottom (n)	-	-	-	-	-	-	-	-	-	-
G1	Top (n)	89.9	6.6	1.1	1.3	0.8	0.1	0.2	-	0.1	3.4
	Bottom (c)	88.6	6.6	1.4	1.7	1.3	0.1	-	-	0.3	4.8
G2	Top (c)	88.4	7.3	1.0	1.4	1.4	0.3	0.1	0.2	0.1	4.4
	Bottom (n)	84.1	6.6	4.1	2.6	2.0	0.3	0.2	0.2	-	9.3

Figure caption

Figure 1. Schematic illustration of the four composite coating series, two multilayer coatings and the other two functionally-graded coating (c: conventional feedstock, n: nanostructured feedstock).

Figure 2. DTA analysis of CMAS-1 (top) and CMAS-2 (bottom).

Figure 3. Raman spectra of: CMAS-1 (a) and CMAS-2 (b).

Figure 4. M2 coating untreated, thermally-treated and attacked by CMAS-1. Top) Micrographs at 500x; bottom) Detail of nanozones (micrographs at 5000x) marked by a square in the top micrographs. Detail of zone chemically attacked surrounded by a square that is amplified in fig. 4. Triangles mark areas where EDX signal is low; stars mark areas where CMAS oxide signal is high.

Figure 5. Detail of a zone chemically attacked by CMAS-1 in M2 coating (star marks a crack and the diamond marks a solid matrix around the zone chemically attacked).

Figure 6. Coatings attacked with the CMAS-1 (micrographs at 500x). Nanozones and zones chemically attacked are marked by squares and circles respectively.

Figure 7. Coatings attacked with the CMAS-2. Nanozones and zones chemically attacked are marked by squares and circles respectively.

Figure 8. Detail of a zone chemically attacked by CMAS-2 in M1 coating (star marks a crack and the diamond marks a solid matrix around the zone chemically attacked).

Figure 9. Left) Raman spectra of M1 coating a) as sprayed; b) thermally-treated; c) attacked with CMAS-1; d) attacked with CMAS-2. Right) Amplification of the Raman spectra around 630 cm^{-1} .

Figure list

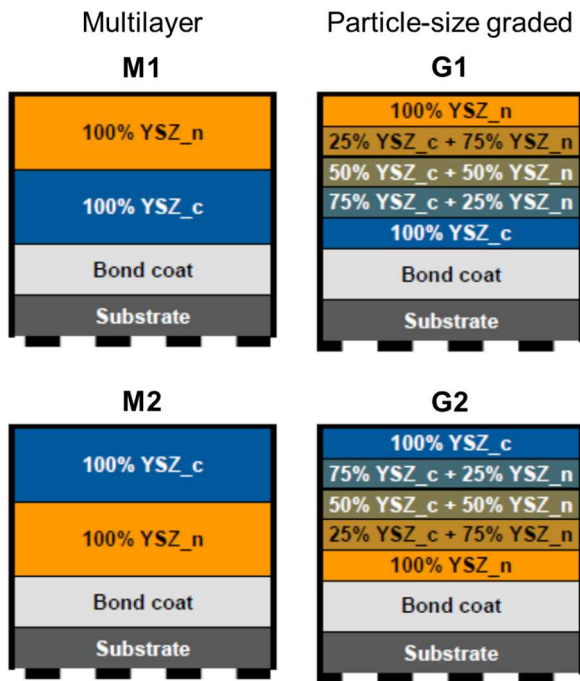


Figure 1

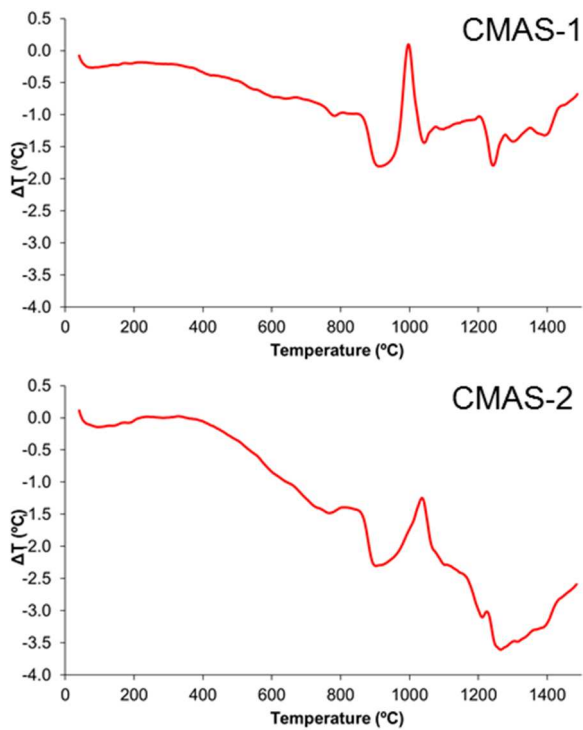


Figure 2

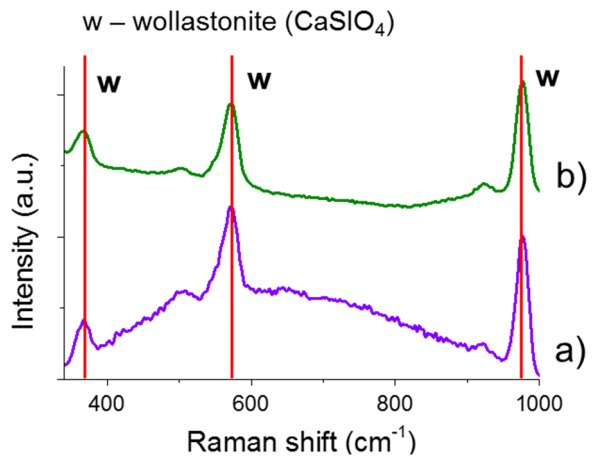


Figure 3

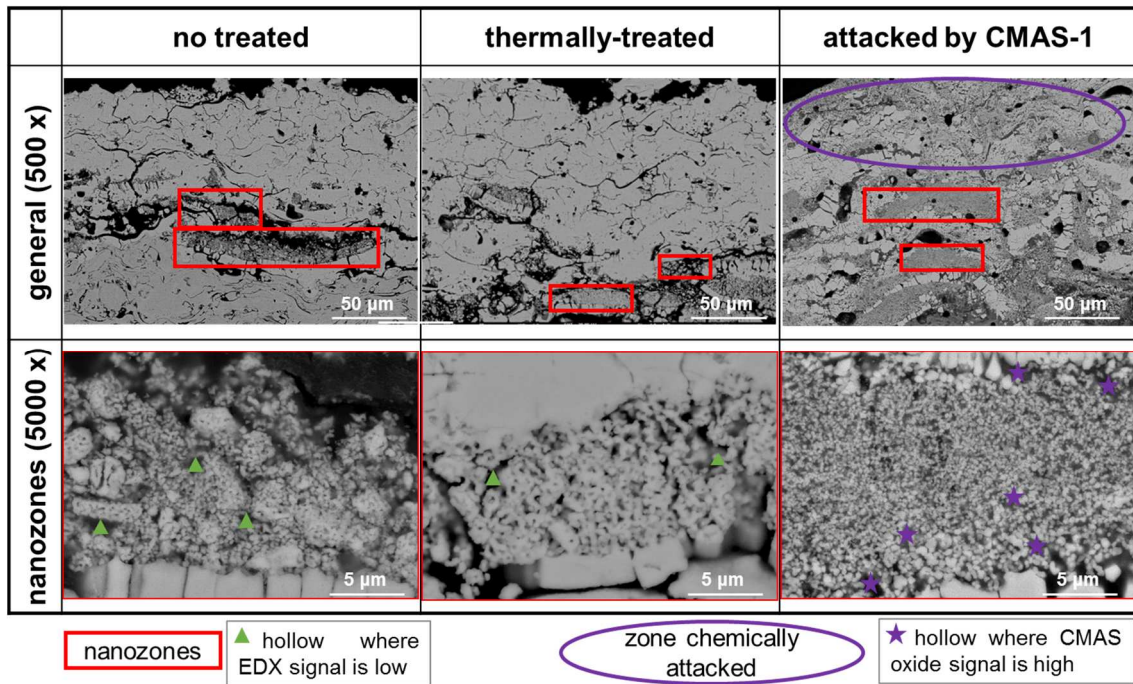


Figure 4

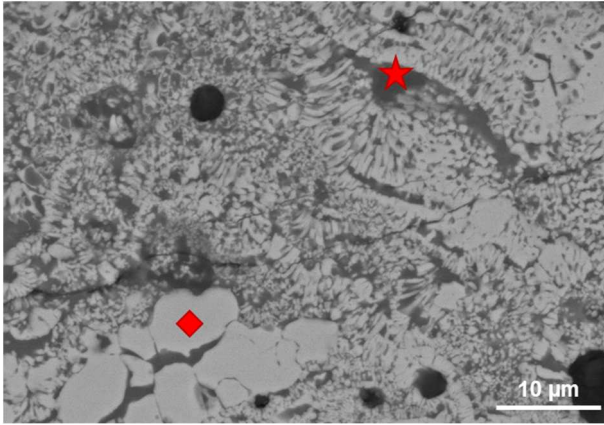


Figure 5

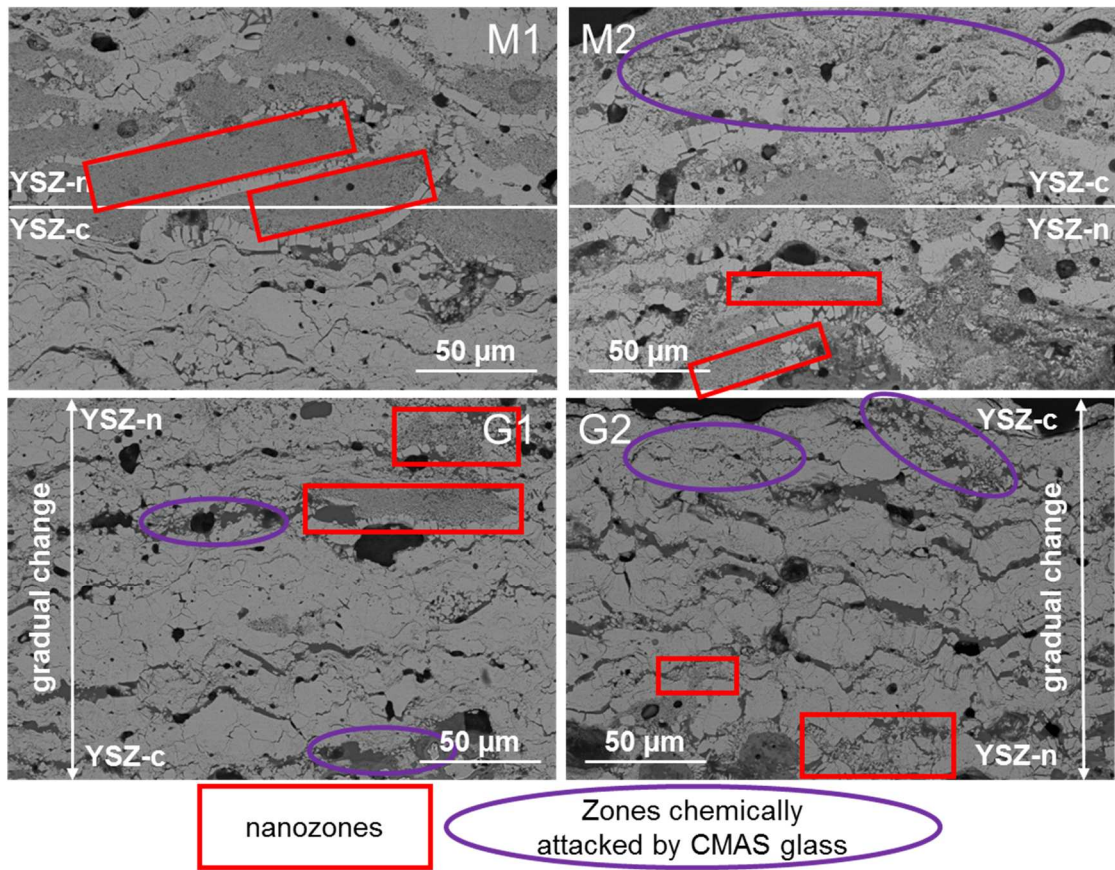


Figure 6

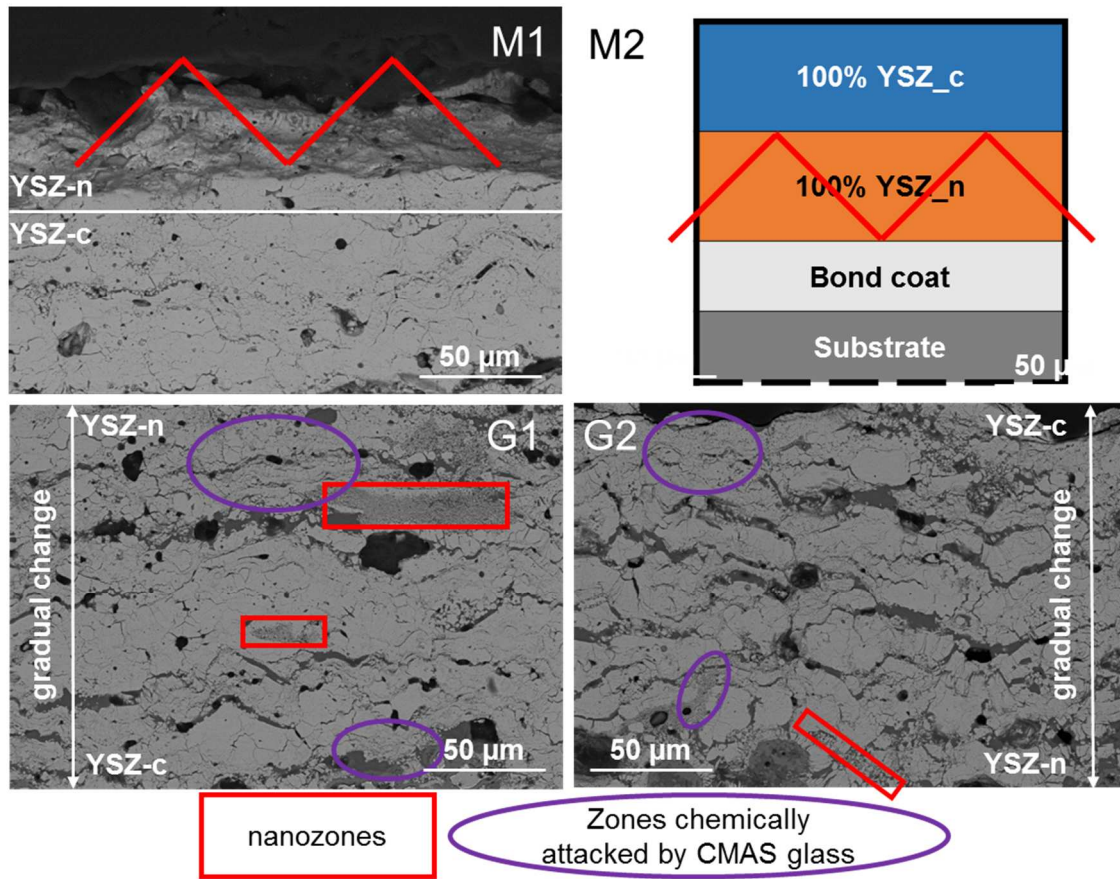


Figure 7

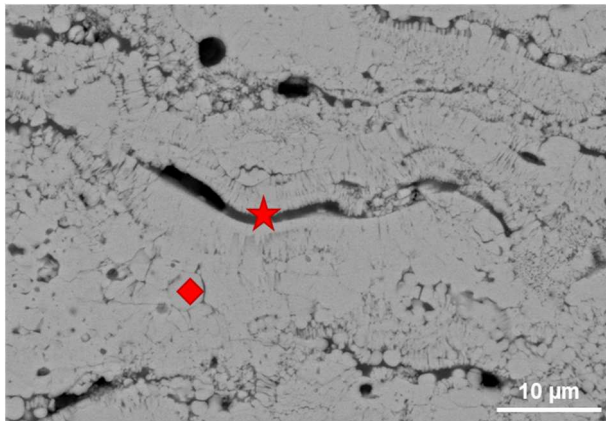


Figure 8

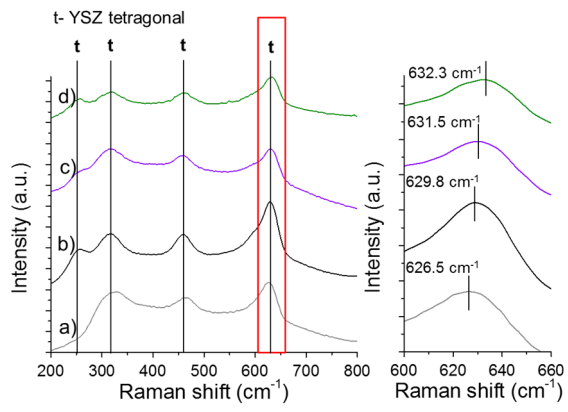


Figure 9